

Article

Application of Hierarchical Clustering Endmember Modeling Analysis for Identification of Sedimentary Environment in the Houtao Section of the Upper Yellow River

Hongli Pang ^{1,*}, Fuqiang Li ², Hongshan Gao ³, Yunxia Jia ⁴, Dianbao Chen ³ and Xiaonan Zhang ⁵ ¹ Department of Tourism Management, Shanghai Maritime University, Shanghai 201306, China² College of Resources and Environment, Gansu Agricultural University, Lanzhou 730070, China; lifq13@lzu.edu.cn³ Key Laboratory of Western China's Environment Systems (Ministry of Education), College of Earth and Environment Science, Lanzhou University, Lanzhou 730000, China; gaohsh@lzu.edu.cn (H.G.); chendb@lzu.edu.cn (D.C.)⁴ School of Geographical Science, Shanxi Normal University, Linfen 041004, China; jiax14@lzu.edu.cn⁵ Institute for Ecological Research and Pollution Control of Plateau Lakes, School of Ecology and Environmental Science, Yunnan University, Kunming 650500, China; zhangxn@ynu.edu.cn

* Correspondence: panghl12@lzu.edu.cn

Abstract: The unmixing of grain-size distribution (GSD) with multivariate statistical analysis provides insight into sediment provenance, transport processes and environment conditions. In this article, we performed hierarchical clustering endmember modeling analysis (CEMMA) to identify the sedimentary environment of fluvial deposits at core HDZ04 drilled in the paleofloodplain on the north bank of the upper Yellow River. The CEMMA results show that four end members can effectively explain the variance in the dataset. End-Member 1 and End-Member 2 are polymodal and dominated by silty clay, and they are associated with the suspended load. End-Member 3 is composed of fine sand and silt, and medium-coarse sand makes up the majority of End-Member 4, corresponding to a mixed saltation load and bed load, respectively. Combined with the end-member scores, we constructed energy values to further divide the core samples into different depositional environments. Unit 2 and unit 5 have a high proportion of coarser end-member components, presenting a shallow channel and a high-energy channel environment, respectively. Unit 1 and unit 3 are composed of fine-grained silt and clay and are dominated by finer end-member components, which can be interpreted as a floodplain situation. Unit 4 is characterized by frequent fluctuations in grain-size composition and energy values, indicating the transition from a high-energy river channel to floodplain deposits. For the channel sedimentary environment, the accumulation rate was relatively low (0.32 mm/yr) due to the frequency migration of the channel. A high accumulation rate of the fluvial deposits had occurred in unit 1 during 1.6 Ka (4.35 mm/yr), which was a response to the influence of increased fluvial instability and human activity during the late Holocene.

Keywords: CEMMA; sedimentary environment; grain-size distribution; Yellow River; fluvial deposits

Citation: Pang, H.; Li, F.; Gao, H.; Jia, Y.; Chen, D.; Zhang, X. Application of Hierarchical Clustering Endmember Modeling Analysis for Identification of Sedimentary Environment in the Houtao Section of the Upper Yellow River. *Water* **2022**, *14*, 1025. <https://doi.org/10.3390/w14071025>

Academic Editors: Zhi-jun Dai and Weiguo Jiang

Received: 25 February 2022

Accepted: 18 March 2022

Published: 24 March 2022

Publisher's Note: MDPI stays neutral with regard to jurisdictional claims in published maps and institutional affiliations.



Copyright: © 2022 by the authors. Licensee MDPI, Basel, Switzerland. This article is an open access article distributed under the terms and conditions of the Creative Commons Attribution (CC BY) license (<https://creativecommons.org/licenses/by/4.0/>).

1. Introduction

As the most important carrier of Earth's surface material migration and the active ecotone among different layers, the fluvial system responds sensitively to changes in regional external conditions [1,2]. In this regard, fluvial sediments record important information concerning the sedimentary environment [3–6]. Particle size is one of the properties of river sediments. Since grain-size parameter equations (median diameter, sorting coefficient, skewness and kurtosis) were proposed by Folk and Ward (1957) [7], increasing attention has been paid to the correlation between sediment particle size and transport conditions [8,9]. Plenty of scholars have analyzed the grain-size parameters of sediments in different sedimentary environments, and based on such statistics, diversified discriminant functions

have been established and widely used in depositional environment discrimination [10–12]. However, the discriminant function may be limited to specific settings without regard to the differences in geomorphic units. As a response to this, some scholars accordingly tried to decompose the grain-size distributions of sediments and infer geological processes in terms of the explanation for the observed variations in grain-size distributions [13,14]. This is because the grain-size characteristics of sediments are the products of multiple factors; the grain-size distribution (GSD) of sediment, controlled by single transportation or the depositional process, is unimodal, and the grain-size distributions in polymodal sediments theoretically reflect different transportation or depositional processes [15]. Based on the above discoveries, the fitting parameter obtained by fitting a defined function formula to the measured GSDs of sediments, by referring to the component score, can simultaneously judge the sedimentary environment [11,12]. By judging the number of peaks, the numerical partitioning of sedimentary components can determine the component number, which, however, results in the deficiency of higher subjectivity [16] or a great difference in scores induced by the same components [17]. Weljie (1997) [18] further proposed that “end-members” represent a series of fixed compositions, which can be regarded as distinct subpopulations within the dataset being analyzed. Statistically, end-members may be defined as a specific (population) setting, corresponding with a certain (frequency distribution) deposition process. Based on multivariate mathematical approaches, EMMA [18], EMMAgeo [19], HALS-NMF [20], BEMMA [21] and CEMMA [22] have been proposed. In recent years, these models have been widely applied to research the relationship of GSD, sedimentary components, the transport medium and the sedimentary environment for loess, aeolian and lacustrine deposits [16,19–23].

The Yellow River is famous for frequent channel migration and for having the highest content of sediment in the world. Under the influence of subsidence tectonic activity, coupled with the distribution of a large number of deserts around the riverbank, the Yellow River has developed a typical desert valley channel in the upper reach [24]. A large amount of geomorphological evidence shows that the Yellow River valley may have developed in the Early Pleistocene [25]. The adjacent desert has experienced multiple expansion–contraction processes accompanied by the migration of the river channel since the Middle Pleistocene [26]. However, the desert landscape in the northern margin of the Ulan Buh desert was formed 2ka ago, and it might respond to lake drying and land desertification caused by the southward migration and abandonment of the Yellow River channel under the influence of human activities [27]. Therefore, reconstruction of the depositional processes is important to understand regional geomorphic evolution. Although the end-member model has previously been applied to analyze fluvial deposits, such as assessing water carrying capacity during flooding [23,28], there is few research on the depositional environment of core sediments. To further extend the end-member model to core sediments and determine its feasibility in sedimentary environment change, we analyzed a sediment core from a desert-wide valley section of the upper Yellow River. Additionally, CEMMA was applied to decompose the grain-size dataset into a certain number of representative components reflecting depositional processes, and we explored the grain-size variation in the fluvial deposits’ response to the sedimentary environment and provenance.

2. Study Area

The Yellow River has a total length of 5464 km, and it can be divided into upper, middle and lower reaches according to its geographical location. The Houtao section is located in the upper reach of the Yellow River from Dengkou to Sanhuhekou, between Lang Mountain to the north and the Ordos Plateau to the south, with a length of 214 km and width ranging from 20 km to 90 km (Figure 1). After Linhe city, the Yellow River flows through the Ulan Buh desert and the Kubuq desert, forming a typical wide-valley desert reach [29]. The river bank on both sides is mainly composed of sand and gravel, and the average gradient is 0.16‰ [30]. As it is located at the fringe of the East Asian monsoon belt,

a temperate continental climate dominates the Houtao Basin, where the mean rainfall is 200–250 mm/yr and potential evaporation capacity is 2000–2300 mm/yr [31].

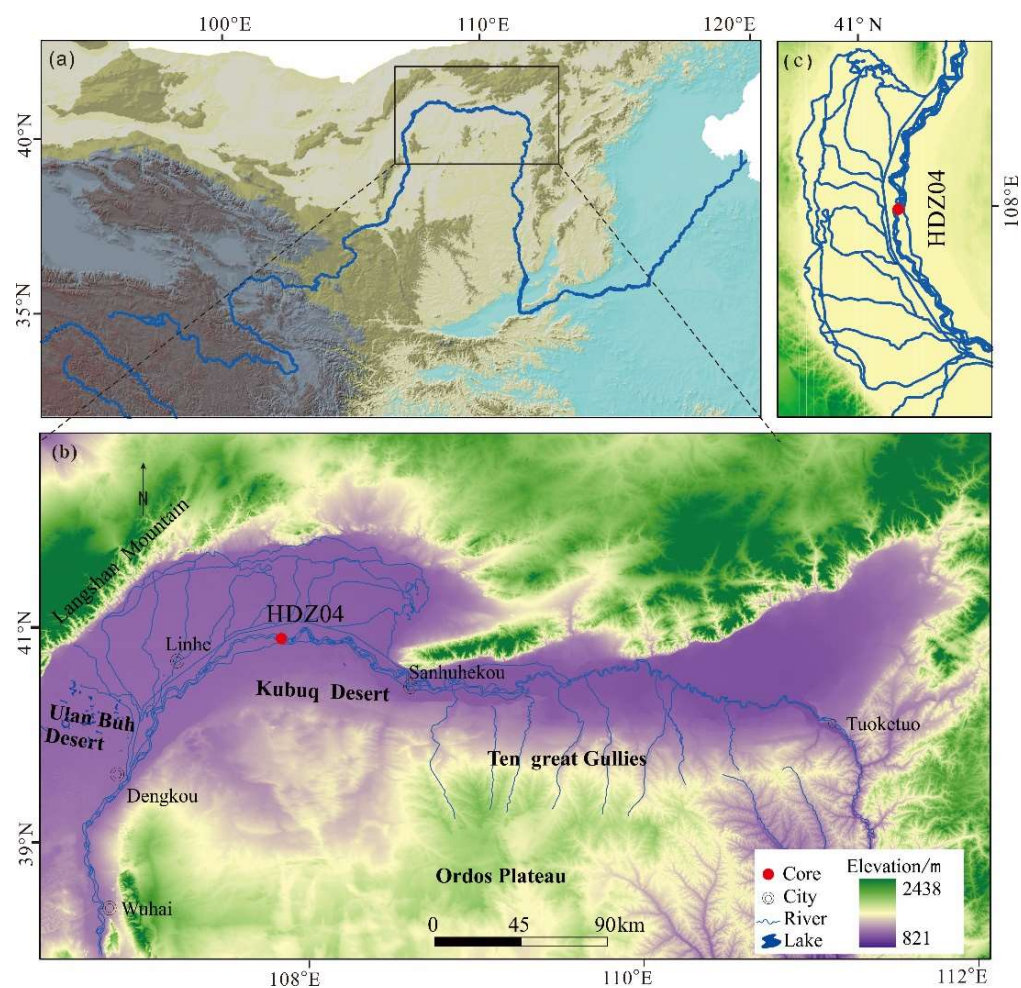


Figure 1. Geographic map of the Yellow River (a). A map showing the location of the Houtao section of the upper Yellow River (b). Site of core (HDZ04) (c).

3. Materials and Methods

3.1. Drill and Sampling

Core HDZ04 ($40^{\circ}51'27.6''$ N, $108^{\circ}02'25.5''$ E) was drilled in the paleofloodplain on the north bank of the modern Yellow River at almost 5 m higher than the river channel. A 22 m-long sediment core was obtained from this site by using the XY-4 geological exploration drilling machine (Huanghai Machinery Factory, Lianyungang, China). Double-layer core tubes were taken to ensure the acquisition of a complete profile.

The length of the recovered core was 18.7 m with an extraction rate of 85%. After being transported to the laboratory, the core was split and subsampled into 5 cm sections at Lanzhou University. The recovered sediments were dominated by sands and could be divided into 5 lithological units from top to bottom (Figure 2).

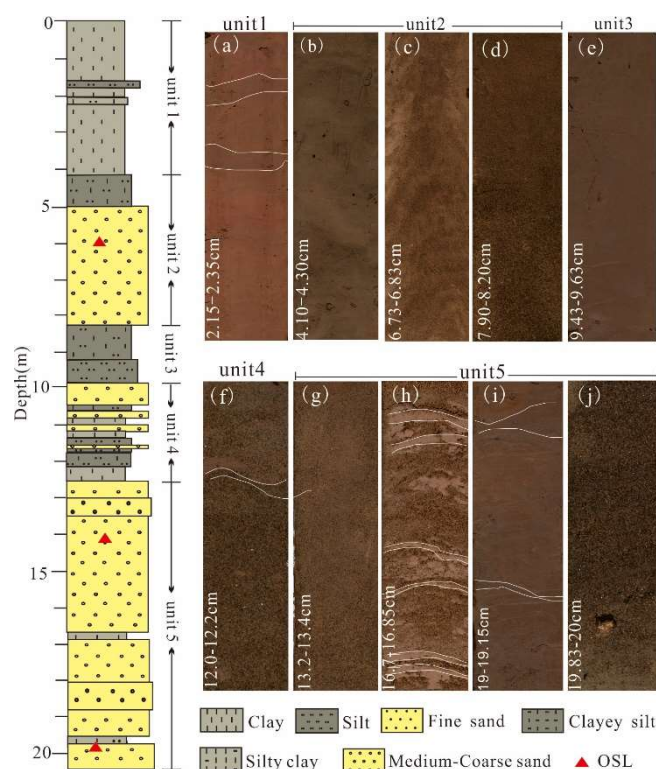


Figure 2. Sediment lithology and core photos. (a) Clay intercalated with thin-layer silt in unit 1. (b) The silt layer and fine sand layer in unit 2. Medium-coarse sand (c) and fining trend of sediments (d) in unit 2. (e) Silt layer of unit 3. (f) Medium-fine sand mix with small amount of clay (white line) in unit 4. (g,h) Fine sand intercalated with thin clay in unit 5. (i) Fine sand mixed with clayey silt in unit 5. (j) Medium-coarse sand layer in unit 5. “OSL” stands for optically stimulated luminescence dating.

Unit 1: 0–4.0 m. This unit was predominantly composed of grayish yellow clay and gray-black silt. The silty clay layer was intercalated with brownish yellow thin-bedded clayey silt.

Unit 2: 4.0–8.3 m. The sediments in this unit were dominated by grayish yellow fine sand and grayish brown medium-coarse sand.

Unit 3: 8.3–9.9 m. In this unit, dark brown silt and clayey silt dominated, mixed with grayish yellow medium-fine sand.

Unit 4: 9.9–12.5 m. This unit mainly consisted of brown silt layers, which were intercalated with thin clay layers.

Unit 5: 12.5–20.41 m. This unit contained grayish yellow fine sand and grayish brown medium-coarse sand, without obvious parallel bedding.

3.2. Grain Size

One hundred eighty-nine samples from HDZ04 were selected at 10 cm resolution for measurements of grain size. We then collected 79 samples from additional sites, which were linked to special depositional environments, including modern riverbed (27), floodplain (20), lacustrine (3) and desert (29) environments. In the field, a self-made sampler was used to collect riverbed sediments along the mainstream of the Yellow River, and the sampling points were at least 10 m away from the riverbank to reduce the impact of human activities. Aeolian samples were gathered from dunes of the Kubuq desert after removing the surface material (~25 cm) to make the samples more representative.

All of the samples were air-dried and analyzed with a Mastersizer 2000 (Malvern Instruments Ltd., Malvern, UK; the measurement range is 0.02–2000 μm). Prior to the measurements, the bulk samples were treated with 30% H_2O_2 and 10% HCl to remove organic materials and carbonate, respectively. Finally, samples were rinsed with deionized

water and mixed with $0.05 \text{ mol L}^{-1} \text{ Na(PO}_3)_6$ on an ultrasonic vibrator for 10 min. We utilized the formula reported by Folk and Ward (1957) [7] to calculate the grain-size composition, median diameter, sorting coefficient, skewness and kurtosis.

3.3. OSL Age

Three samples for optically stimulated luminescence (OSL) dating were extracted in tubes from any silt and fine sand layer of the core, before being transported to the laboratory for analysis in opaque anti-sunlight bleaching containers. The OSL samples were opened under a subdued red light in the luminescence dating laboratory. From the material in the unexposed middle parts of the cores and tubes, quartz with a 38–63 μm fraction was extracted for luminescence measurements. Pre-processing was performed with reference to the study conducted by Li et al. (2018) [32]. OSL signal measurements were made using an automated Risø TL/OSL-DA-15 reader (DTU Physics, Lyngby, Denmark). Equivalent dose (De) measurements were measured using a combination of the Single-Aliquot Regenerative (SAR) dose protocol [33] and the Standard Growth Curve (SGC) method [34], namely, the SAR-SGC method [35]. We used similar De measurement conditions and annual dose measurements from previous studies in this area [32] for all luminescence samples investigated in this study. The values for De as well as the total dose rates for these samples are given in Table 1.

Table 1. The age–depth of core HDZ04.

Depth (m)	K (%)	Th (ppm)	U (ppm)	Water Content (%)	Dose Rate (Gy/ka)	De (Gy)	OSL Age (ka)
6.1	1.54 ± 0.07	8.51 ± 0.26	1.89 ± 0.14	22 ± 5	2.2 ± 0.17	3.01 ± 0.21	1.4 ± 0.1
14.2	1.47 ± 0.06	5.1 ± 0.19	1.18 ± 0.13	15 ± 5	1.94 ± 0.16	51.14 ± 1.49	26.3 ± 0.23
19.9	1.53 ± 0.06	4.47 ± 0.18	1.09 ± 0.13	21 ± 5	1.72 ± 0.14	51.21 ± 1.53	29.7 ± 2.5

3.4. Hierarchical Clustering End-Member Modeling Analysis (CEMMA)

The end-member model was first proposed by Weltje (1997) [18], who proposed that the compositional variation in GSD was caused by the mixing of material from different sources (end members). The relationship can be expressed as a linear mixing model:

$$X = M_{(n \times Q)} B_{(Q \times P)} + E_{(n \times P)} \quad (1)$$

where matrix $M_{(n \times Q)}$ is the proportional contribution of the end member; $B_{(Q \times P)}$ represents the composition matrix, and $E_{(n \times P)}$ represents the errors of the model. In this model, n is the sample number, P is the variable parameters, and Q is the end number.

CEMMA can be regarded as a nonparametric statistic of GSDs, which infer the number of end members using agglomeration coefficients. Then, the city-block distance is used to quantify the similarity between GSDs, and it is expressed as the following [21]:

$$d_{(ij)} = \sum_{k=1}^p |x_{ik} - x_{jk}| \quad (2)$$

where $d_{(ij)}$ represents the distance between the GSD of x_i and x_j , and p is the number of size classes in each GSD. High values of $d_{(ij)}$ indicate a lower degree of similarity between curves x_i and x_j , whereas a value close to 0 suggests extreme similarity. We merge the most similar pair of clusters into a new cluster according to $d_{(ij)}$, and we repeat this step until all clusters are combined into one cluster.

$$d_{(rs)} = \min d_{(ij)} \quad (3)$$

The unmixed GSDs are defined as the most typical GSDs in the dataset that are representative of their clusters.

$$C_{(q)} = \min d_{(q,ks)} \quad (4)$$

Theoretically, the number of end members and their compositions can be determined accurately, and the contributions of end members to each sample can be estimated using standard least-squares techniques [18]. Under the principle of mass conservation, the fraction of each end member should be nonnegative, and the sum is close to 1 [36].

$$\sum_{k=1}^q m_{ik} = 1 \quad (5)$$

where m_{ik} indicates the contribution of each end member, and q is the number of the end member. The grain-size distributions of 189 samples in the HDZ04 were transformed to end members using CEMMA in order to further explore the information about the depositional environment contained within the grain-size distribution.

4. Results

4.1. Grain-Size Characteristics of Core HDZ04

The core deposits are mainly composed of silt (56.7%) and sand (35.2%), as well as a small amount of clay (8.1%) (Figure 3). The frequency histogram shows that the median diameters of the sediments are between 5 μm and 304 μm , and the proportion of particles with a median diameter larger than 100 μm is 51%. The grain-size parameters indicate that these sediments are mainly characterized by positive skewness, and a medium or sharp and narrow distribution of kurtosis curves. In addition, the sorting coefficients of the sediments range from 0.46 to 3.17, thus classifying them as primarily medium to poorly sorted, with a small amount being well sorted (2%). Furthermore, the sediments with a median diameter of less than 100 μm are characterized as poorly sorted, and they are dominated by a sharp and narrow distribution of kurtosis curves, while the coarse particles (100–329 μm) show a large fluctuation, partially dominated by relatively very well sorted and symmetric skewness. The samples in unit 1 are characterized by multimodal GSDs with a high proportion of silt-sized particles. The GSDs in unit 2 show two modes, and the sorting degree is better than that of unit 1. The samples from unit 3 are medium-to-coarse silts, with a dominant mode size range from 30 μm to 70 μm . In unit 4, the sediments are characterized by a higher content of coarse-sized particles with unimodal GSDs and a low content of fine-sized particles (mode at 10–30 μm). The sediments in unit 5 are composed of fine-to-medium sand with a dominating mode of 100–300 μm . Importantly, the GSDs of the sediments are similar to those of the coarse-sized particles in unit 4, which could be interpreted as representing a depositional environment similar to that of unit 4.

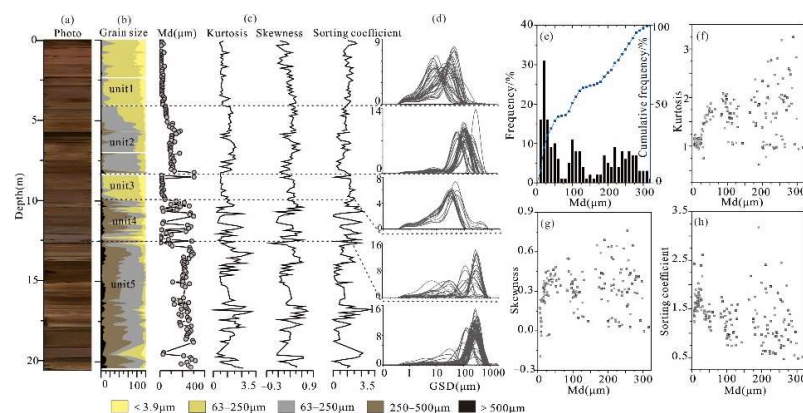


Figure 3. (a) High-resolution photos of core HDZ04 were taken by the XRF in situ scanner. (b) Grain-size composition of core sediments. (c) Grain-size parameters of core sediments in HDZ04. (d) Grain-size distributions of sediments in the different units. (e) Frequency distribution histogram and cumulative frequency of median diameter in HDZ04. (f) Plots of median diameter and kurtosis (f), sorting coefficient and median diameter (g), median diameter and skewness (h) in core sediments.

4.2. End-Member Analysis

The median coefficient of determination (r^2) reveals that a four-end-member model, which can reproduce ~85% of the total variance of the GSDs, is the most suitable mixing model for the core HDZ04 dataset. EM1 is characterized by polymodal distribution with a high proportion of fine-sized particles, and the grain size ranges from 1 μm to 100 μm (Figure 4). In addition, EM1 is composed of an obvious mode and two secondary modes. It has a dominant mode at 30 μm , and the secondary mode corresponds to 0.6 μm (clay) and 5 μm (silt). The cumulative frequency curve of the grain size shows that the intercept point of the saltation and suspended components is between 4 ϕ and 5 ϕ , and the suspended component accounts for more than 70%, indicating that EM1 is positioned in a low-energy hydrodynamic condition. EM2 has a mode at 51 μm (silt) and a secondary mode at 60 μm . The cumulative probability curve of the grain size has two phases. The intercept point of the saltation and suspension components is near to 4 ϕ , and, it occupies almost 50% of the suspension component. The GSD of EM3 ranges from 0.1 to 300 μm ; it has a dominant mode at 121 μm (fine sand); and its saltation component is slightly higher than that of EM2. The coarsest labeled EM4 has a bimodal GSD with modes at 40 μm and 284 μm . The intercept point of the saltation and suspension components is near to 3 ϕ , and the saltation component is more than 90%, which demonstrates strong dynamic conditions.

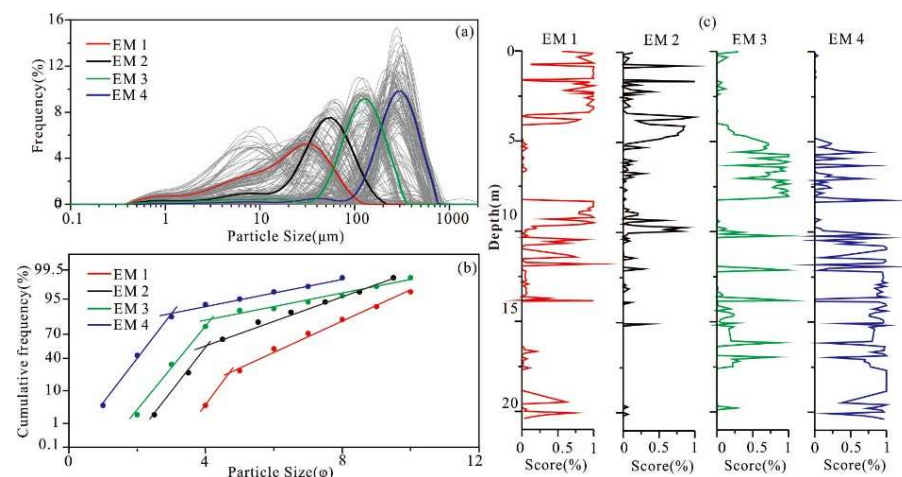


Figure 4. The hierarchical clustering endmember modeling analysis results. (a) Grain-size distributions (GSDs) of samples from sediment core HDZ04 and the GSDs of four endmember (colored lines) by the CEMMA. (b) Probabiity cumulative curves for four endmember. (c) End-member score (%).

The relative contributions of the four EMs appear to fluctuate with their stratigraphic position (Table 2). EM1 is dominant in unit 1 and unit 2, with its contribution reaching over 90%. Contrary to EM1, EM2 has a lower contribution to unit 1 and unit 2 (17%), and the contribution of EM2 gradually decreases from 23% to 0% after 9.9 m. EM3 accounts for an average of 67% in unit 3, and it quickly declines from 67% to 1% in unit 4. However, the average contribution of EM4 increases after 8.3 m, and the contribution reaches 56% and 84% in unit 4 and unit 5, respectively. In general, EM1 and EM2 are dominantly presented in unit 1 and unit 3, which mainly consist of fine silt and clay, while EM3 and EM4 account for more than 90% in unit 2 and unit 5.

Table 2. The grain-size composition of core HDZ04 and the average scores of the four EMs in relation to depth.

Unit	Depth (m)	Mz (μm)	Sand %	Silt %	Clay %	P _{EM1}	P _{EM2}	P _{EM3}	P _{EM4}
1	0–4.0	18.1	7.5	75.7	16.8	0.80	0.17	0.02	0.00
2	4.0–8.3	104	71	25.3	3.7	0.01	0.17	0.67	0.15
3	8.3–9.9	41.5	9.6	76.1	14.3	0.74	0.23	0.01	0.02
4	9.9–12.5	147.4	60.5	31.1	8.4	0.28	0.02	0.13	0.56
5	12.5–20.4	217.8	86.6	10.1	3.3	0.04	0.01	0.10	0.84

5. Discussion

5.1. Interpretation of End Members

It has long been recognized that the GSDs of sediments are polymodal and represent different transport or depositional processes [8,16,37]. Under hydraulic environments with a specific energy, sediments are mainly transported by three modes, namely, bed load, saltation and suspension modes, depending on their particle size, with settlement occurring as the transport rate gradually decreases [38]. For example, aeolian sediments are dominated by the coarse-grain saltation group, and hydraulic sediments are dominated by overlapping coarse and fine components with specific grain-size ranges, which, according to dynamic estimation, are saltation and suspension groups, respectively [8,15]. The GSDs of known sediments from different depositional environments of the Yellow River are shown in Figure 5. Aeolian sediment presents unimodal distribution and spans the size range of 0–550 μm , with the mode being 200–300 μm . The GSDs of fluvial sediments are mainly bimodal, with the primary mode ranging from 50 μm to 200 μm and the secondary mode from 1 μm to 10 μm . Alluvial floodplain sediments are characterized by bimodal or multimodal distribution, and the mode ranges from 30 μm to 70 μm . The GSDs of lacustrine (fluvial overflow lacustrine) sediments show multimodal distribution, consisting of fine-grained particles within the range of 1–100 μm . Based on the GSDs of the sediments described above, the mode sizes of sediments gradually become small from the aeolian sand, fluvial and floodplain to lacustrine samples, as suggested by Sun et al. (2002) [38].

Among the four end members, EM1 is the finest and has a polymodal distribution positioned in the silt and clay range. Figure 4 shows that the highest EM1 scores are found in the surface layer. Compared with the GSDs of modern sediments, the GSD of EM1 is similar to that of lacustrine sediments. EM2 is dominated by fine-grained silt, with the mode being 60 μm . The cumulative probability curve of EM2 indicates that the proportion of the suspended group is almost 50%, and the saltation component increases compared with that of EM1, which is comparable to the modern floodplain samples. Furthermore, the changing trend of EM2 and EM1 with depth is clearly similar, and high values mainly occur in the sedimentary units that are dominated by clay and silt. The total sum of EM1 and EM2 reaches an amount exceeding 85%, and, therefore, it is reasonable to hypothesize that EM1 and EM2 experienced weak hydraulic conditions, which is interpreted as suspended load. EM3 is mainly composed of fine sand (63–125 μm), with a sharp and narrow primary mode (size 100–200 μm) and an unobvious secondary mode. As for EM3, the percentage of the saltation component reaches 80%, and its sorting is better than that of EM1 and EM2, representing a strong hydrodynamic condition. Thus, we can safely argue that EM3 can be associated with fluvial saltation or bed-load deposits. EM4 is mainly composed of coarse sand, with a primary modal size of 100–300 μm , which resembles the GSDs of samples from the fluvial deposits at the Hanzhong Basin [39]. EM4 also coincides with the grain size range of aeolian sediment. However, the GSDs of aeolian sediment are commonly unimodal, without a fine tail distribution, which is the same as that of EM4. One probable explanation is that EM4 represents a mixture of fluvial bed-load deposits and aeolian deposits.

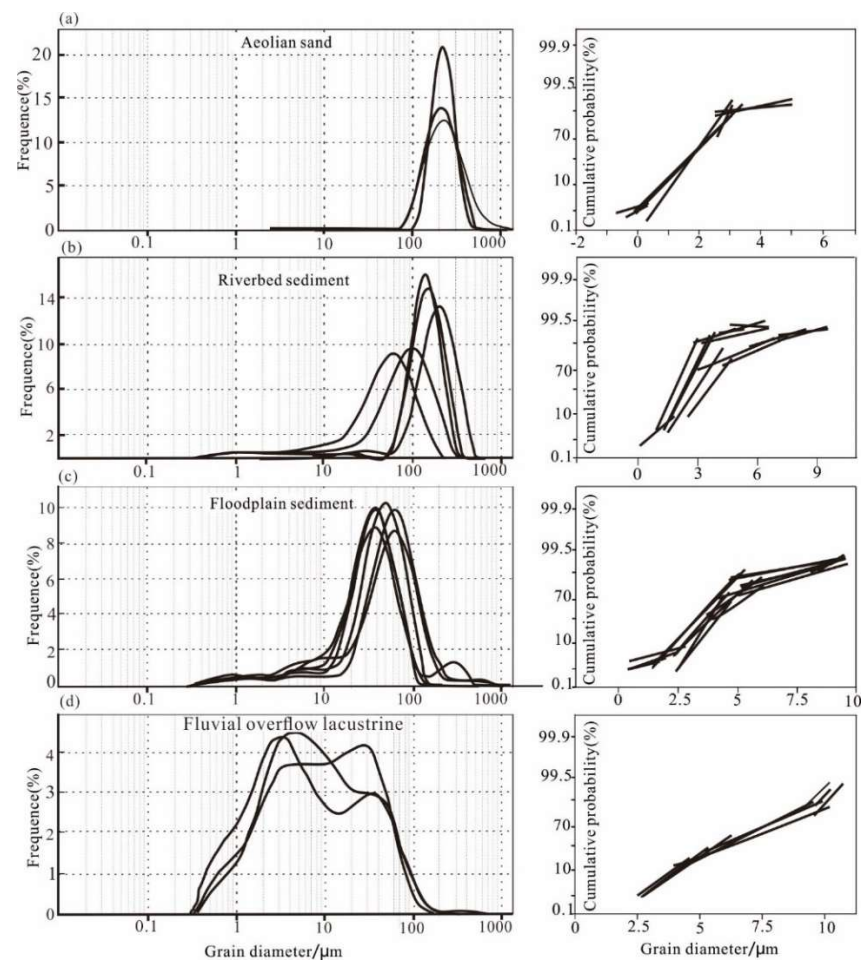


Figure 5. Grain-size distributions and Probability cumulative curves of sediments from different sedimentary environments. (a) GSDs of aeolian sand. (b) GSDs of riverbed sediments. (c) GSDs of sediments from floodplain environment. (d) GSDs of sediments from fluvial overflow environment.

5.2. Reconstruction of Depositional Environment in HDZ04

Fluvial sediments have a typical binary structure, which can be divided into channel and floodplain deposits. However, it seems impossible for us, by analyzing drill cores, to provide direct deposition information as in the field profile, and, therefore, examining sediment structure characteristics, such as particle size, is a common technique that is used to analyze sedimentary strata [40]. Particle size is closely related to transport intensity, and related indexes, such as particle size parameters, C-M plots and GSDs, are widely used to reconstruct fluvial depositional conditions [41]. In HDZ04, the GSDs of the fine end members (EM1 and EM2) are distinct from those of the coarse end members (EM3 and EM4), indicating different deposition processes. EM1 and EM2 can be interpreted as sediments primarily in the form of suspension movement, and, similarly, the coarse components EM3 and EM4 can be regarded as saltation or bed-load components; this interpretation refers to the study conducted by Erkens et al. (2013) [42]. Consequently, we constructed the total value of EM1 + EM2 and EM3 + EM4 to highlight the contribution of the fine component and the coarse component, respectively. High values (50–100%) indicate high-energy conditions, while lower values (0–49%) reflect low-energy conditions. Combined with the CEMMA results and core lithology, the vertical sedimentary sequence of HDZ04 was reconstructed (Figure 6).

In unit 5, the GSDs of the sediments are characterized as unimodal in the coarse component. In addition, EM4 dominates most of the sediment in this unit; thus, the total sum of EM3 and EM4 is higher than 95%, implying a high-energy fluvial condition. For sediments

from a depth of 16.7 m–16.85 m, their thick sand layer was mixed with clay particles (Figure 6c), indicating a sandy channel environment during a period of a high-energy flood. Notably, some samples from unit 5 are distinctly well sorted. For example, samples from a depth of 14.4–14.9 show a sorting coefficient range from 0.52 to 0.59 (Figure 6h). Therefore, we infer that the well-sorted coarse particles are not from the upper channel based on the landscape setting of the study area [29,43] but, rather, that they are probably from the proximal desert. In winter, desert sand is accumulated in the gullies when the tributary shrinks or dries up completely, and during the rainy season, floods carry desert sand flows into the Yellow River in the form of hyperconcentrated flows. After entering the channel, fine particles primarily deposit in the floodplain by suspension transport, while coarse particles (100–300 μm) basically deposit in the riverbed. Because of coupled wind–water processes, the reworked desert sand can be regarded as a mixture of aeolian and hydraulic sediments, which is verified by the bimodal GSD of EM4. Unit 4 presents an irregular fining trend, with a proportion of EM4 decreasing and EM1 (silt group) increasing. This may be correlated with a reduction in the fluvial contribution and an increase in the floodplain component. We conclude that unit 4 is formed during the frequent interaction of a shallow channel with a floodplain environment. Meanwhile, some of the samples that are well sorted are similar to those of aeolian sediments (Figure 6g), suggesting that aeolian sand settled in the channel and was reworked by wind action. In unit 3, the total sum of EM1 and EM2 is 97%, and median size of sediments is finest (Figure 6f), which can be regarded as a low-energy floodplain environment. Unit 2 is characterized by a relatively high value of EM3, but low EM4 can be distinguished by the high-energy samples in unit 5. In addition, the particle sizes of the sediment in unit 2 show an upward decrease (Figure 6e), indicating a gradual reduction in the contribution of channel deposits. Thus, unit 2 can be assumed to be a shallow channel to a low-energy floodplain. The GSDs of samples in unit 1 are similar to those in unit 3, and they consist of lowly sorted fine components (Figure 6d), which can be regarded as a low-energy floodplain.

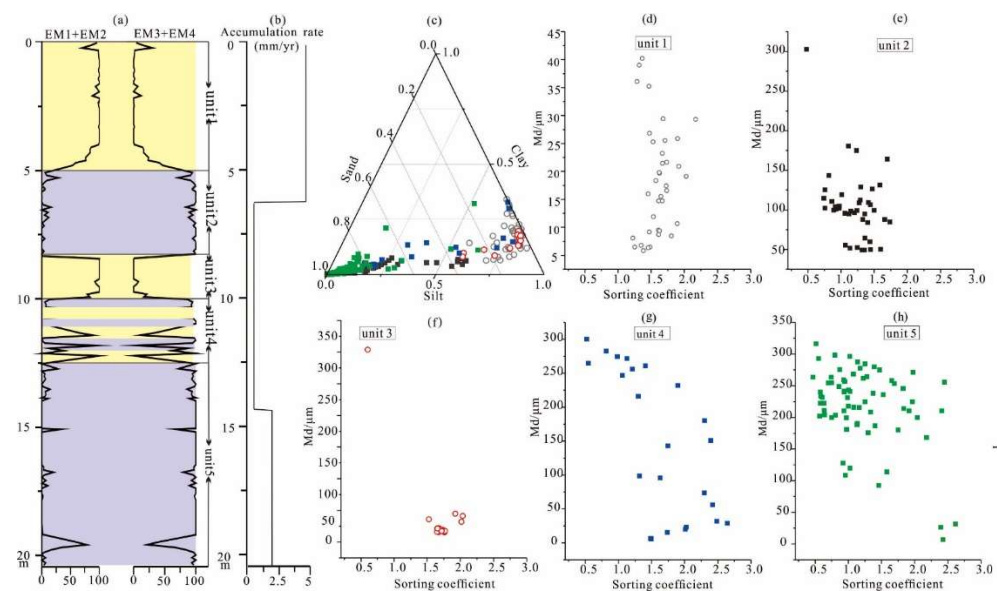


Figure 6. Sedimentary sequence of fluvial deposits at HDZ04. (a) Energy values are calculated by the total value of EM3 and EM4 or EM1 and EM2. (b) Accumulation rate of fluvial deposits. (c) grain-size composition of sediments from different units in HDZ04. Relationships between median diameter and sorting coefficient in sediments from unit 1 (d), unit 2 (e), unit 3 (f), unit 4 (g) and unit 5 (h).

5.3. Evolution of Depositional Environment

There are five units, and they form the high-energy channel, transitional environment, floodplain environment, shallow channel and floodplain depositional environment, implying fining-upward sedimentary cycles in HDZ04 at the Houtao alluvial plain. High-energy

channel deposits (EM3) dominantly contribute to unit 2, flowing by the low-energy floodplain environment (EM1 and EM2) in unit 1 (Figure 6a). Reworked aeolian sediments (EM4) distribute at the lower part of the sedimentary sequence (Figure 4). In the alluvial plain, the depositional environment of sediments changes frequently in the longitudinal profile, which, in response to the shaping process of the plain, mainly includes the lateral point-bar aggradation and the vertical aggradation of the river channel and floodplain, which is often changed by channel migration or lateral migration [44]. As the channel gradually became inactive, the coarse component could not be carried, and the channel was abandoned, resulting in fine-sized particles covering the paleochannel [37]. This evolution can reveal the fining-upward sedimentary sequence of HDZ04. Accordingly, unit 5 reflects a period of an active fluvial flood, when aeolian sediments deposited in the channel and formed a thick layer of sand-sized particles. However, in unit 2, there is very little reworking of aeolian sediments accumulated in the river channel, which may be caused by the low activity of the channel. For the aeolian sediments in unit 4 (EM4), one might be from the same flood input as those in unit 5, and others may be reworked within the floodplain environment [45].

Changes in the sedimentary environment also influence the sedimentation rate. The Houtao Basin has experienced persistent sedimentation since the Quaternary, with an average annual deposition rate of 0.4 mm/yr [31]; however, the sedimentation rate of unit 4 is only 0.32 mm/yr (Figure 6b). The slow accumulation rate of the channel deposits might have been caused by the frequent migration of the river channel, and as a result, the formed silt/clay floodplain layers were repeatedly eroded. There is a phenomenon where the accumulation rate rapidly increased to 4.35 mm/yr since 1.6 Ka (Figure 6b), when the Yellow River was dominated by a floodplain sedimentary environment. The floodplain deposits were relatively stable, especially in the alluvial plain, and their sedimentary interruption was easier to record compared to other sedimentary units. Therefore, the younger the depositional age, the less the sedimentary discontinuity is recorded, and the accumulation rate of floodplain deposits will increase. This is proven by the rapid increase in the late Holocene deposition rate all over the world [46,47]. In addition, human activities in the Houtao section of the Yellow River have aggravated land desertification since 2 Ka [48], leading to significant increases in material in the channel, which is one of the reasons for the rapid accumulation rate.

6. Conclusions

This paper reconstructs the sedimentary environment of HDZ04 by using the CEMMA method in the Houtao section of the upper Yellow River. The results show that the core sediments were mainly composed of four end members. The modal sizes of EM1 and EM2 corresponded to 30 μm and 51 μm , with the modes of EM3 and EM4 being 121 μm and 284 μm , respectively, all shedding light on the suspension and saltation/bed-load processes. Combined with the GSDs of modern sediments and the results of four EMs, the core was divided into a high-energy channel, transitional environment, floodplain environment, shallow channel and floodplain sedimentary environment. Preliminary classification of fluvial sedimentary facies in HDZ04 was carried out, which provided an improved method for the identification of sedimentary processes using a combination of the CEMMA method and the grain size of modern sediments. We think this study is capable of deciphering robust sediment components of the fluvial sediment system and has potential to be a standard method when similar challenges are encountered elsewhere. Hence, this method can be further used in grain-size analysis to study other kinds of sedimentary environments. Concerning the complexity of the fluvial system, the original grain-size information might be affected by a combination of processes. Therefore, multi-source modern surface samples are essential to ensure the accuracy of the results.

Author Contributions: Conceptualization, H.P.; methodology, H.G.; software, X.Z.; validation, F.L., Y.J. and D.C.; formal analysis, H.P.; investigation, H.P.; writing—original draft preparation, H.P.; writing—review and editing, H.P. and F.L.; supervision, H.G. All authors have read and agreed to the published version of the manuscript.

Funding: This research was supported by the National Natural Science Foundation of China (Grant No. 42001004; 42001008; 42041006).

Institutional Review Board Statement: Not applicable.

Informed Consent Statement: Not applicable.

Data Availability Statement: Not applicable.

Acknowledgments: The authors thank the editor and anonymous reviewers, for their constructive suggestions and linguistic improvement. We thank Joffrey Bertaz for revising the language.

Conflicts of Interest: The authors declare no conflict of interest.

References

1. Coulthard, T.J.; Macklin, M.G. How sensitive are river systems to climate and land-use changes? A model-based evaluation. *J. Quat. Sci.* **2001**, *16*, 347–351. [[CrossRef](#)]
2. Apollaro, C.; Marini, L.; De Rosa, R.; Settembrino, P.; Scarciglia, F.; Vecchio, G. Geochemical features of rocks, stream sediments, and soils of the Fiume Grande Valley (Calabria, Italy). *Environ. Geol.* **2007**, *52*, 719–729. [[CrossRef](#)]
3. Singh, P.; Rajamani, V. Geochemistry of the Floodplain Sediments of the Kaveri River, Southern India. *J. Sediment. Res.* **2001**, *71*, 50–60. [[CrossRef](#)]
4. Radoane, M.; Radoane, N.; Dumitriu, D.; Crina Miclaus, C. Downstream variation in bed sediment size along the East Carpathian rivers: Evidence of the role of sediment sources. *Earth Surf. Processes Landf.* **2008**, *33*, 674–694. [[CrossRef](#)]
5. Snelder, T.H.; Lamouroux, N.; Pella, H. Empirical modelling of large scale patterns in river bed surface grain size. *Geomorphology* **2011**, *127*, 189–197. [[CrossRef](#)]
6. Walling, D.E. The evolution of sediment source fingerprinting investigations in fluvial systems. *J. Soil Sediments* **2013**, *13*, 1658–1675. [[CrossRef](#)]
7. Folk, R.L.; Ward, W.C. Brazos river bar A study in the significance of grain size parameters. *J. Sediment. Petrol.* **1957**, *27*, 3–26. [[CrossRef](#)]
8. Ashley, G.M. Interpretation of polymodal sediments. *J. Geol.* **1978**, *86*, 411–421. [[CrossRef](#)]
9. Bagnold, R.A.; Barndorff-Nielsen, O. The pattern of natural size distributions. *Sedimentology* **1980**, *27*, 199–207. [[CrossRef](#)]
10. Sahu, B.K. Depositional Mechanisms from the Size Analysis of Clastic Sediments. *J. Sediment. Res.* **1964**, *34*, 73–83.
11. Sheridan, M.F.; Wohletz, K.H.; Dehn, J. Discrimination of grain size subpopulations in pyroclastic deposits. *Geology* **1987**, *15*, 367. [[CrossRef](#)]
12. Shih, S.; Komar, P.D. Sediments, beach morphology and sea cliff erosion within an Oregon coast littoral cell. *J. Coast. Res.* **1994**, *10*, 144–157.
13. Prins, M.A.; Vriend, M.; Nugteren, G.; Vandenberghe, J.; Lu, H.; Zheng, H.; Wetje, G.J. Late Quaternary aeolian input variability on the China Loess Plateau: Inference from unmixing of loess grain-size records. *Quat. Sci. Rev.* **2007**, *26*, 230–242. [[CrossRef](#)]
14. Van Hateren, J.A.; Prins, M.A.; Balen, R.V. On the genetically meaningful decomposition of grain-size distributions: A comparison of different end-member modelling algorithms. *Sediment. Geol.* **2017**, *375*, 1–23. [[CrossRef](#)]
15. Middleton, G.V. Hydraulic interpretation of sand size distributions. *J. Geol.* **1976**, *84*, 405–426. [[CrossRef](#)]
16. Ijmker, J.; Stauch, G.; Hartmann, K.; Diekmann, B.; Dietze, E.; Opitz, S.; Wünnemann, B.; Lehmkuhl, F. Environmental conditions in the Donggi Cona lake catchment, NE Tibetan Plateau, based on factor analysis of geochemical data. *J. Asian Earth Sci.* **2012**, *44*, 176–188. [[CrossRef](#)]
17. Paterson, G.A.; Heslop, D. New methods for unmixing sediment grain size data. *Geochem. Geophys. Geosyst.* **2015**, *16*, 4494–4506. [[CrossRef](#)]
18. Wejse, G.J. End-member modeling of compositional data Numerical-statistical algorithms for solving the explicit mixing problem. *Math. Geol.* **1997**, *29*, 503–549. [[CrossRef](#)]
19. Dietze, E.; Hartmann, K.; Diekmann, B.; Ijmker, J.; Lehmkuhl, F.; Opitz, S.; Stauch, G.; Wünnemann, B.; Borchers, A. An end-member algorithm for deciphering modern detrital modern processes for lake sediments of Lake Donggi Cona, NE Tibetan Plateau, China. *Sediment. Geol.* **2012**, *243*, 169–180. [[CrossRef](#)]
20. Yu, S.; Colman, S.M.; Li, L. BEMMA: A Hierarchical Bayesian End-Member Modeling Analysis of sediments grain size distributions. *Math. Geosci.* **2016**, *48*, 723–741. [[CrossRef](#)]
21. Zhang, X.; Zhou, A.; Wang, X.; Song, M.; Zhao, Y.; Xie, H.C.; Russell, J.M.; Chen, F. Unmixing grain size distribution in lake sediments: A new method of end member modeling using hierarchical clustering. *Quat. Res.* **2018**, *89*, 365–373. [[CrossRef](#)]
22. Andrews, J.T.; Eberl, D.D. Determination of sediment provenance by unmixing the mineralogy of source-area sediments: The “SedUnMix” program. *Mar. Geol.* **2012**, *291–294*, 24–33. [[CrossRef](#)]
23. Peng, F.; Prins, M.A.; Kasse, C.; Cohen, K.M.; Van der Putten, N.; Van der Lubbe, J.; Toonen, W.; Ban, R.T. An improved method for paleoflood reconstruction and flooding phase identification, applied to the Meuse River in the Netherlands. *Glob. Planet. Change* **2019**, *177*, 213–224. [[CrossRef](#)]

24. Wang, S.J.; Yan, Y.X.; Li, Y.K. Spatial and temporal variations of suspended sediment deposition in the alluvial reach of the upper Yellow River from 1952 to 2007. *Catena* **2012**, *92*, 30–37. [[CrossRef](#)]
25. Hu, Z.B.; Pan, B.T.; Guo, L.Y.; Vandenberghe, J.; Liu, X.; Wang, J.; Fan, Y.; Mao, J.; Gao, H.; Hu, X. Rapid fluvial incision and headward erosion by the Yellow River along the Jinshaan gorge during the past 1.2 Ma as a result of tectonic extension. *Quat. Sci. Rev.* **2016**, *133*, 1–14. [[CrossRef](#)]
26. Li, G.Q.; Jin, M.; Chen, X.M.; Wen, L.; Zhang, J.; Madsen, D.; Zhao, H.; Wang, X.; Fan, T.; Duan, Y.; et al. Environmental changes in the Ulan Buh Desert, southern Inner Mongolia, China since the Middle Pleistocene based on sedimentology, chronology and proxy indexes. *Quat. Sci. Rev.* **2015**, *128*, 69–80. [[CrossRef](#)]
27. Li, F.Q.; Gao, H.S.; Zhang, L.K.; Li, Z.M.; Pang, H.L.; Pan, B.T. Grain size Characteristics and Evolution of Core Sedimentary Environment in the Houtao Plain Reach of the Yellow River. *Acta Sedimentol. Sin.* **2019**, *37*, 1234–1243. (In Chinese with English abstract) [[CrossRef](#)]
28. Toonen, W.T.G.; Winkels, T.G.; Cohen, K.M.; Prins, M.A.; Middelkoop, H. Lower Rhine historical flood magnitudes of the last 450 years reproduced from grain-size measurements of flood deposits using End Member Modelling. *Catena* **2015**, *130*, 69–81. [[CrossRef](#)]
29. Ta, W.Q.; Wang, H.B.; Jia, X.P. Downstream fining in contrasting reaches of the sand-bedded Yellow River. *Hydrol. Process.* **2011**, *25*, 3693–3700. [[CrossRef](#)]
30. Wang, S.J. Analysis of River Pattern Transformations in the Yellow River Basin. *Process Geogr.* **2008**, *27*, 10–17. (In Chinese with English abstract)
31. Yang, G.S.; Ta, W.Q.; Dai, F.N. Contribution of sand sources to the silting of riverbed in Inner Mongolia section of Huanghe River. *J. Desert Res.* **2003**, *23*, 152–159. (In Chinese with English abstract) [[CrossRef](#)]
32. Li, F.Q.; Pan, B.T.; Lai, Z.P.; Gao, H.S.; Ou, X.J. Identifying the degree of luminescence signal bleaching in fluvial sediments from the Inner Mongolian reaches of the Yellow River. *Geochronometria* **2018**, *45*, 82–96. [[CrossRef](#)]
33. Murray, A.S.; Wintle, A.G. Luminescence dating of quartz using an improved single-aliquot regenerative-dose protocol. *Radiat. Meas.* **2000**, *32*, 57–73. [[CrossRef](#)]
34. Lai, Z.P. Testing the use of an OSL standardised growth curve (SGC) for De determination on quartz from the Chinese Loess Plateau. *Radiat. Meas.* **2006**, *41*, 9–16. [[CrossRef](#)]
35. Lai, Z.P.; Ou, X. Basic procedures of optically stimulated luminescence (OSL) dating. *Prog. Geogr.* **2013**, *32*, 683–693. (In Chinese with English abstract) [[CrossRef](#)]
36. Weltje, G.J.; Prins, M.A. Genetically meaningful decomposition of grain-size distributions. *Sediment. Geol.* **2007**, *202*, 409–424. [[CrossRef](#)]
37. Vandenberghe, J. Grain size of fine-grained windblown sediment: A powerful proxy for process identification. *Earth-Sci. Rev.* **2013**, *121*, 18–30. [[CrossRef](#)]
38. Sun, D.; Bloemendal, J.; Rea, D.K.; Vandenberghe, J.; Jiang, F.; An, Z.; Ruixia, S. Grain-size distribution function of polymodal sediments in hydraulic and aeolian environment, and numerical partitioning of the sedimentary component. *Sediment. Geol.* **2002**, *152*, 263–277. [[CrossRef](#)]
39. Yang, X.; Wang, X.Y.; Balen, R.V.; Prins, M.; Wang, S.J.; Buuren, U.V.; Lu, H.Y. Fluvial terrace formation and its impacts on early human settlement in the Hanzhong Basin, Qingling mountains, central China. *Glob. Planet. Change* **2019**, *178*, 1–14. [[CrossRef](#)]
40. Walker, R.G.; Cant, D.J. Sandy fluvial systems. *Facies Models* **1984**, *1*, 71–89.
41. Kanhaiya, S.; Singh, B.P.; Tripathi, M.; Sahu, S.; Tiwari, V. Lithofacies and particle-size characteristics of late Quaternary floodplain deposits along the middle reaches of the Ganga river, central Ganga plain, India. *Geomorphology* **2016**, *284*, 220–228. [[CrossRef](#)]
42. Erkens, G.; Toonen, W.H.J.; Cohen, K.M.; Prins, M.A. *Unravelling Mixed Sediment Signals in the Floodplains of the Rhine Catchment Using End Member Modelling of Grain Size Distributions*; University of Leeds: Leeds, UK, 2013; pp. 109–110.
43. Pang, H.L.; Pan, B.T.; Garzanti, E.; Gao, H.S.; Zhao, X.; Chen, D.B. Mineralogy and geochemistry of modern Yellow River sediments: Implications for weathering and provenance. *Chem. Geol.* **2018**, *488*, 76–86. [[CrossRef](#)]
44. Dunne, T.; Mertes, L.A.K.; Meade, R.H.; Richey, J.E.; Forsberg, B.R. Exchanges of sediment between the flood plain and channel of the Amazon River in Brazil. *GSA Bull.* **1998**, *110*, 450. [[CrossRef](#)]
45. Vandenberghe, J.; Sun, Y.B.; Wang, X.Y.; Abel, H.A.; Liu, X.X. Grain-size characterization of reworked fine-grained aeolian deposits. *Earth-Sci. Rev.* **2018**, *177*, 43–52. [[CrossRef](#)]
46. Hoffmann, T.; Erkens, G.; Gerlach, R.; Klostermann, J.; Lang, A. Trends and controls of Holocene floodplain sedimentation in the Rhine catchment. *Catena* **2009**, *77*, 96–106. [[CrossRef](#)]
47. Macklin, M.G.; Jones, A.F.; Lewin, J. River response to rapid Holocene environmental change: Evidence and explanation in British catchments. *Quat. Sci. Rev.* **2010**, *29*, 1555–1576. [[CrossRef](#)]
48. Li, B.Y.; Ge, Q.S.; Zheng, J.Y. Evolution of the Yellow River in the Houtao plain of Inner Mongolia in the past 2000 years. *Acta Geogr. Sin.* **2003**, *58*, 239–246. (In Chinese with English abstract)